

Chemical Science

Accepted Manuscript

This article can be cited before page numbers have been issued, to do this please use: L. He, J. He, E. Chen and Q. Lin, *Chem. Sci.*, 2024, DOI: 10.1039/D4SC04063E.



This is an Accepted Manuscript, which has been through the Royal Society of Chemistry peer review process and has been accepted for publication.

Accepted Manuscripts are published online shortly after acceptance, before technical editing, formatting and proof reading. Using this free service, authors can make their results available to the community, in citable form, before we publish the edited article. We will replace this Accepted Manuscript with the edited and formatted Advance Article as soon as it is available.

You can find more information about Accepted Manuscripts in the [Information for Authors](#).

Please note that technical editing may introduce minor changes to the text and/or graphics, which may alter content. The journal's standard [Terms & Conditions](#) and the [Ethical guidelines](#) still apply. In no event shall the Royal Society of Chemistry be held responsible for any errors or omissions in this Accepted Manuscript or any consequences arising from the use of any information it contains.

ARTICLE

Boosting Photothermal Conversion through Array Aggregation of Metalloporphyrins in Bismuth-based Coordination Frameworks

Liang He,^a Jing He,^a Er-Xia Chen,^{*a,c} and Qipu Lin^{*a,b,d}Received 00th January 20xx,
Accepted 00th January 20xx

DOI: 10.1039/x0xx00000x

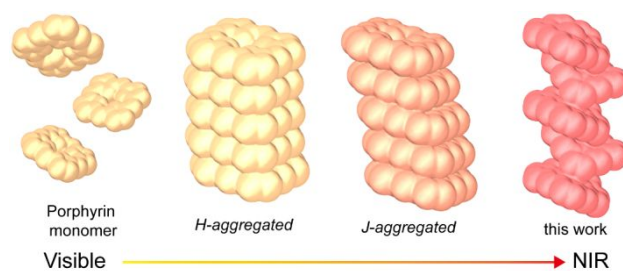
Materials capable of efficiently converting near-infrared (NIR) light into heat are highly sought after in biotechnology. In this study, two new three-dimensional (3D) porphyrin-based metal-organic framework (MOFs) with a *sra*-net, viz. CoTCCP-Bi/NiTCCP-Bi, were successfully synthesized. These MOFs feature bismuth carboxylate nodes interconnected by metalloporphyrinic spacers, forming one-dimensional (1D) arrays of closely spaced metalloporphyrins. Notably, the CoTCCP-Bi exhibits an approximate Co...C distance of 3 Å, leading to enhanced absorption of NIR light up to 1400 nm due to the presence of strong interlayer van der Waals forces. Furthermore, the spatial arrangement of the metalloporphyrins prevents axial coordination at the centers of porphyrin rings and stabilizes a Co^{II}-based metalloradical. These characteristics promote NIR light absorption and non-radiative decay, thereby improving photothermal conversion efficiency. Consequently, CoTCCP-Bi can rapidly elevate the temperature from room temperature to 190 °C within 30 seconds under 0.7 W cm⁻² energy power from 808 nm laser irradiation. Moreover, it enables solar-driven water evaporation with an efficiency of 98.5% and a rate of 1.43 kg m⁻² h⁻¹ under 1 sun irradiation. This research provides valuable insights into the strategic design of efficient photothermal materials for effective NIR light absorption, leveraging the principles of aggregation effect and metalloradical chemistry.

Introduction

Light-to-heat conversion materials have garnered significant attention for their potential applications in biomedicine, actuators, catalysis, and solar steam generation.¹ Recent advancements have led to the emergence of a diverse array of photothermal materials, including carbon-based composites, metal-based inorganic materials, organic molecules and polymers, as well as inorganic-organic hybrids.² The Jablonski diagram illustrates that improving the photothermal effect requires enhancements in the material's light absorption, especially in near-infrared (NIR) absorption, as well as the optimization of its non-radiative transition process, which involves energy dissipation and simultaneous heat generation.³ In addition, radical-based materials offer unique benefits for achieving efficient photothermal conversion owing to the existence of unpaired electrons and their spin effects.⁴ However, radicals are highly chemically reactive, making the

actual preparation of photostable photothermal materials with a wide light absorption range challenging.

The self-assembly of organic molecules through aggregation greatly facilitates the development of NIR photothermal materials by inducing a red-shifted spectral absorption.⁵ Porphyrin, a prototypical π -conjugated organic molecule, is increasingly recognized as a promising candidate for photothermal conversion due to its tunable optical properties and reactivity.⁶ While monomeric porphyrin has limitations in terms of NIR absorption and photothermal conversion efficiency, the broadening and red-shifting of the absorption peak can be achieved by forming suitable aggregates through interactions such as π - π stacking, electrostatic attraction, or hydrogen bonding.⁷ For instance, compared to the head-to-head approach of porphyrin *H*-aggregates, the head-to-tail configuration of *J*-aggregates results in stronger electronic coupling between molecules,



Scheme 1. Enhanced light absorption caused by different ways of porphyrinic aggregation.

^a State Key Laboratory of Structural Chemistry, Fujian Institute of Research on the Structure of Matter, Chinese Academy of Sciences, Fuzhou 350002, China

^b University of Chinese Academy of Sciences, Beijing 100049, China

^c Fujian Science & Technology Innovation Laboratory for Optoelectronic Information of China, Fuzhou, Fujian 350108, China

^d State Key Laboratory of Photocatalysis on Energy and Environment, Fuzhou University, Fuzhou, Fujian 350116, China.

† Supplementary Information (ESI) available: detailed experimental procedures, X-ray crystallographic data (CCDC #2323214, and #2356520), and additional structural and characterizing figures (PXRD, TGA, FT-IR, SEM, EPR, stability analysis, adsorption-desorption isotherms, UV-Vis DRS, photoluminescence, photothermal conversion experiments, etc.). See DOI: 10.1039/x0xx00000x



leading to absorption redshift (Scheme 1).⁸ Additionally, metallized porphyrin endows advantages for NIR light absorption. The coordination of metal ions in porphyrin rings can significantly alter the orbital hybridization within the porphyrin chromophore.^{4b,9} This modification may alleviate the spin prohibition of porphyrin's Q bands, thereby enhancing light absorption and causing red shifting. Furthermore, the presence of metal ions in porphyrin rings can directly influence axial bonding and interactions between porphyrins in aggregates, potentially boosting light absorption and stabilizing metal radicals.

A variety of spectroscopic techniques and theoretical models are employed to unravel the impact of metalloporphyrin aggregation on NIR light absorption enhancement. Nevertheless, the random arrangement and amorphous nature of most multi-metalloporphyrin assemblies present challenges in achieving a comprehensive understanding of the underlying principles using these methods.¹⁰ Therefore, there is considerable interest in transitioning metalloporphyrin-based disordered aggregates to crystalline phases, which offer well-defined and customizable structures that allow for the investigation of the role of metalloporphyrin aggregation mode in enhancing NIR light absorption at the molecular or atomic scale. Metalloporphyrin-based metal-organic frameworks (MOFs) have emerged as class of crystalline materials with potential applications due to their precise spatial arrangement of components, tunable structures, and excellent light harvesting capabilities, rendering them an ideal platform for studying the role of metalloporphyrin aggregation in photothermal conversion.¹¹ However, current design strategies for metalloporphyrin-based MOFs primarily concentrate on optimizing porosity to increase gas sorption or exposing active sites (e.g., metalloporphyrin centers) to enhance catalytic performance, often leading to the spatial separation of active centers and limiting the investigation of metalloporphyrin stacking patterns in MOFs.¹²

The efficient incorporation of densely packed metalloporphyrins into a MOF necessitates the selection of appropriate metal nodes and porphyrin ligands. The bismuth(III) oxidation state proves particularly advantageous due to its high coordination numbers and flexible coordination environments, enabling the creation of unique metal complexes with distorted conformations of inorganic building blocks (IBUs).¹³ Additionally, bismuth and its complexes are non-toxic, making them appealing for diverse applications such as sea water desalination, medicine and biotechnology.¹⁴ Herein, we have successfully fabricated two bismuth-metalloporphyrin-based MOF, denote as MTCPP-Bi, TCPP = tetra(4-carboxyphenyl)porphyrin, M = Co^{II} and Ni^{II}), which consist of a one-dimensional (1D) rod-like aggregation of Co/NiTCPP (Figure 1). The stacking pattern between porphyrins resembles the head-to-tail pattern typical of *J*-aggregates, albeit forming a helix. The strong Bi-O bonds and stacking force between adjacent metalloporphyrin moieties impart excellent chemical tolerance to MTCPP-Bi. Furthermore, the aggregation of metalloporphyrins and the

abundance of Co^{II}-based metalloradicals contribute to the broad light absorption of CoTCPP-Bi, extending into the NIR-II range. These attributes position CoTCPP-Bi as a promising candidate for photothermal conversion applications.

Results and discussion

Synthetic procedures

All the samples can be formed in capped vials (see the Supporting Information – SI for details). Their phase purities and formulas were confirmed by X-ray diffraction (XRD), elemental and thermogravimetric analyses, scanning electron microscopy (SEM), electron paramagnetic resonance (EPR), Fourier transformed-infrared (FT-IR) and ultraviolet-visible (UV-Vis) diffuse reflection spectroscopy, fluorescence (ESI[†]).

Structures and characterizations of MTCPP-Bi

CoTCPP-Bi and NiTCPP-Bi were prepared using the solvothermal method, with a detailed protocol provided in the Supporting Information (SI, Section S1.2). Single-crystal X-ray diffraction (XRD) analysis revealed that both CoTCPP-Bi and NiTCPP-Bi share an identical framework structure, possessing a three-dimensional (3D) structure with twofold interpenetration, aligned with the $P2_12_12$ space group (Figure 1a, Table S1). During the solvothermal procedure, Co^{II} or Ni^{II} metalated the porphyrinic macrocycles (TCPP) at their centers to be MTCPP that served as a four-connection square planar node (Figure 1c), linking with four-connection [Bi(COO)₄] IBUs to create a *sra*-net (Figures 2d and S1). The molar ratio of Co^{II}/Ni^{II} -to-Bi^{III} was determined as 1:1 through site occupancy refinement, considering the distinct X-ray scattering factors and coordination environments of the metals. Metal content was validated by inductively coupled plasma-mass spectrometry (ICP-MS), element mapping images (Figure S4), energy dispersive spectroscopy (EDS) (Figures S5 and S6), and Fourier-transform infrared spectroscopy (FT-IR) (Figure S7). X-ray photoelectron spectroscopy (XPS) confirmed the local coordination environment of M^{II} in MTCPP-Bi (Figures S8 and S9). The N1s XPS of CoTCPP-Bi showed identical binding energies (1087 eV) to CoTCPP, in contrast to the notable shifts in metal-free TCPP. Additionally, the Co2p binding energies for CoTCPP and CoTCPP-Bi remained consistent at 692 eV and 708 eV, respectively, with the Co2p binding energy peak absent in unmetallized TCPP. Similarly, the binding energies of N and Ni in both NiTCPP and NiTCPP-Bi samples are nearly identical, with Ni positioned at 855 eV and 872 eV, and N at 398 eV (Figure S10). These findings attest to the successful metallization of TCPP by Co^{II} or Ni^{II} during the *in-situ* synthesis of MTCPP-Bi. The unusual spatial arrangement of metalloporphyrins contributes to the specific twist angle and parallel orientation of IBUs within the interwoven networks, generating a continuous 1D rod-like aggregation facilitated by offset π - π interactions (Figures 1b and 1c).



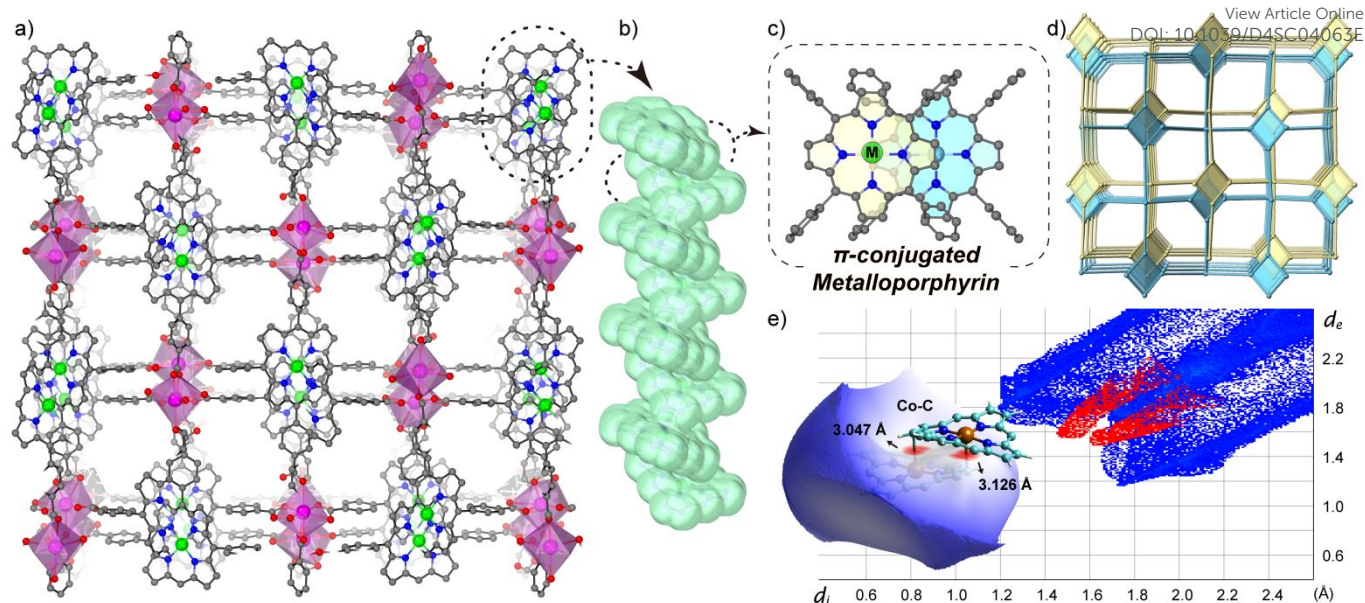


Figure 1. (a) Crystal structure of MTCPP-Bi viewed along the *c* axis. (b) Side view and (c) top view of 1D rod-like aggregation of MTCPP in MTCPP-Bi, illustrating the orbital overlap area between neighbouring porphyrin macrocycles. (d) Twofold interpenetrated network with *sra* topology. (e) Hirshfeld surface analysis and fingerprint plots for CoTCCP-Bi. M = Co/Ni in (a) and (c).

The close proximity of adjacent metalloporphyrins enhances π - π interactions, resulting in a substantial increase in interlayer orbital overlap. Noteworthy, a strong interaction exists between the metal cobalt at the core of the porphyrin ring and the pyrrole β -carbon of the axially neighboring porphyrin layer, evidenced by a compressed metal-carbon (Co...C) distance of only 3 Å (Figure. S2). This distance is significantly smaller than the Ni...C distance in the NiTCCP-Bi (minimum, 3.3 Å). In addition, the Co...C distance is shorter than the standard van der Waals contact observed in prior studies between graphite layers (3.4 Å) and adjacent porphyrins (> 3.2 Å).¹⁵ As unveiled through investigations in the crystal database CCDC, the discovery of M...C contact within porphyrin aggregates marks a new finding. However, this distance is too long to denote coordination interaction, as it exceeds the length of robust M-C covalent bonds found in compounds like alkylco-balamins (1.99–2.03 Å),¹⁶ as well as Co-C (C60, < 2.7 Å)¹⁷ in the neutral complexes of fullerenes with metal-incorporating porphyrins. To gain deeper insights into the interlayer interactions in CoTCCP-Bi, density functional theory (DFT) calculations were utilized to examine the noncovalent interactions (NCIs) between adjacent metalloporphyrins in CoTCCP-Bi. Real-space visualization of both attractive and repulsive interactions in the structure, based on electron density, indicates that neighboring metalloporphyrins exhibit interlayer van der Waals interactions involving the porphyrin rings and peripheral benzene rings (Figure S11). Additionally, the analysis of density of states (DOS) displays a significant overlap between adjacent layers within the bonding region, indicating pronounced interlayer interactions (Figure S12). Fingerprint maps and further analysis of these interactions suggest that the stronger van der Waals forces originate from the metal-mediated

interaction, specifically between cobalt and carbon (Figure 1e). The electrostatic potential (ESP) analysis demonstrates that the presence of Co causes distortion in the electron density at the porphyrin core, and the aggregation of cobalt porphyrins facilitates a cohesive arrangement of 1D porphyrin arrays (Figure S13). In brief, the theoretical investigation underscores that the unique stacking pattern of metalloporphyrins engenders robust interlayer van der Waals interactions, indicative of a strong intermolecular interaction among neighboring metalloporphyrinic linkers and holding promise in elucidating the electronic and optical properties of the underlying porphyrin assemblies.

Metalloporphyrins typically aggregate in a 1D manner; however, the structures of MTCPP-Bi exhibit open square channels with aperture dimension of $9.1 \times 5.8 \text{ \AA}^2$. Pore characteristics were assessed using PLATON software, revealing small solvent-accessible voids with a volume of 1953 \AA^3 , accounting for 21.1% of the unit cell volume. Despite pre-activation to remove lattice solvents, N_2 adsorption-desorption isotherms of MTCPP-Bi at 77 K showed no detectable uptake, which could be attributed to blockage of porous channels by residual guest molecules, rendering the MOF inoperative for N_2 sorption. Nonetheless, the permanent porosity of the representative CoTCCP-Bi was validated through CO_2 capture measurements at 195 K, demonstrating a type-I isotherm indicative of microporous behavior (Figure S14). The Brunauer-Emmett-Teller (BET) surface area of CoTCCP-Bi was determined to be $464 \text{ m}^2 \text{ g}^{-1}$. CoTCCP-Bi maintains structural integrity in aqueous solutions spanning a pH range of 3 to 12 (Figure S15), and remains stable in some common organic solvents such as methanol, *N,N*-dimethylformamide (DMF), acetonitrile, toluene, *n*-hexane, and acetone, as confirmed by powder XRD (PXRD) (Figure S16). Its thermal stability,



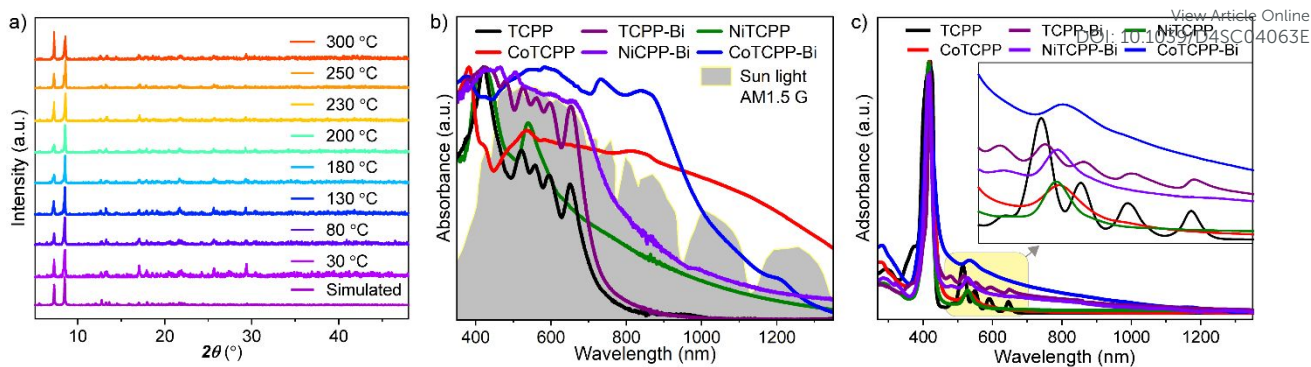


Figure 2. (a) Temperature-dependent PXRD patterns of CoTCPP-Bi under air atmosphere. (b) UV-Vis-NIR absorption spectra of powder samples of TCPP, TCPP-Bi, NiTCPP, CoTCPP, NiTCPP-Bi, CoTCPP-Bi, and the solar spectral irradiance (AM 1.5 G), and (c) their solutions in DMF.

evaluated using thermogravimetry (TG) and temperature-dependent PXRD, suggests that the framework of CoTCPP-Bi remains intact when exposed to air up to 300 °C (Figures 2a and S17).

To explore the influence of metallization and aggregation modes of porphyrins on light absorption, we chose a 2D layered structure named Bi-TCPP for comparative testing (Figure S3).¹⁸ In Bi-TCPP, which is composed of TCPP organic ligands and Bi³⁺ inorganic nodes, only interlayer van der Waals interactions occur between the peripheral benzene ring and the central porphyrin rings due to the dislocated assignment of neighboring layers. The UV-Vis-NIR absorption spectra of powdered samples, including TCPP, TCPP-Bi, NiTCPP, CoTCPP, NiTCPP-Bi, and CoTCPP-Bi, are depicted in Figure 2b. Compared to the monomeric TCPP, TCPP-Bi shows a noteworthy enhancement in light absorption up to 800 nm. Both the metalloporphyrin Co/NiTCPP and their assemblies, Co/NiTCPP-Bi, exhibit absorption peaks that extend into the NIR-II region (1400 nm). To further clarify the impact of metallization, importantly, the absorption intensity of CoTCPP-Bi is greatly higher than that of the nickel-metalized samples. This expanded absorption range of CoTCPP-Bi closely matches the energy distribution of sunlight (AM1.5G simulated sunlight), effectively covering a substantial portion of the solar spectrum (Figure S18). The presence of Co^{II} and the short distance between the metalloporphyrin linkers may contribute to this outcome. Prior research indicates that the spin-allowed d-d transition of cobalt, characteristic of a Co^{II} complex, enhances the NIR absorption of the sample.¹⁹ we conducted liquid mapping on light absorption and spectral absorption tests in a DMF solution (Figure 2c). Compared with TCPP and TCPP-Bi, the changes in the position and quantity of the Q-band peaks of CoTCPP, NiTCPP, CoTCPP-Bi, and NiTCPP-Bi after metallization could be attributed to the asymmetry induced by the metal centers. The absorption spectra of TCPP-Bi, CoTCPP-Bi, and NiTCPP-Bi display a wider range of absorption compared to TCPP, CoTCPP, and NiTCPP. This broadening is partly attributed to the distinct molecular arrangements in solution: TCPP, CoTCPP, and NiTCPP are present as individual molecules in DMF, whereas TCPP-Bi, CoTCPP-Bi, and NiTCPP-Bi are dispersed as aggregates, which introduces scattering effects.

Density functional theory calculations, and EPR characterization

The role of metalloporphyrin aggregation on light absorption was further investigated through DFT calculations. The molecular geometry was optimized using the PBE0 functional. Figure 3a clearly illustrates the profiles of the singly occupied molecular orbitals (SOMO) and singly unoccupied molecular orbitals (SUMO) for both the α and β spins of CoTCPP and CoTCPP-Bi. For the open-shell CoTCPP and CoTCPP-Bi, the majority of frontier orbitals are ligand-centered, and the calculated low energy bands primarily arise from π - π^* transitions. Additionally, the contribution of cobalt to SUMO (β) suggests the involvement of d orbitals of the central metal in light absorption. This phenomenon is also noted in CoTCPP-Bi, where the aggregation of cobalt porphyrins promotes orbital overlap, reducing the band gap between SOMO and SUMO. The calculated band gap decreases from 2.89 eV for CoTCPP to 2.54 eV for CoTCPP-Bi, broadening the spectral region to sunlight. These results emphasize the significant influence of metalloporphyrin aggregation behavior on electronic spectra. To further examine the electronic structures of CoTCPP and CoTCPP-Bi, electron spin density was computed using the Multiwfn program (Figure 3b). Analysis of spin distributions uncovered a predominance of single electrons on the central cobalt, followed by cobalt-coordinated nitrogen atoms, indicating the existence of a Co^{II}-based metalloradical. Bulk samples were subjected to variable-temperature continuous-wave X-band EPR spectroscopy, showing a signal at approximately 3300 G with $g = 2.00$ at 100 K, as depicted in Figure 3c. Similar signals have been observed in other porphyrins and associated with organic π -radicals based on carbon and nitrogen.²⁰ Notably, Cobaltous-porphyrin is a low-spin Co^{II}-complex with a lone unpaired electron in the 3d orbital, making this unpaired electron highly sensitive to alterations in the axial coordination of the metal ion. External molecules like O₂ induce a distortion of the coordination and adjust the oxidation state of Co, potentially forming Co-O₂ adducts identified as Co^{III} superoxo (O₂⁻) species.²¹ In addition, ligating molecules such as oxygen increase the electron density on Co, akin to the effect of an N base in cobaltous-porphyrin systems. Consequently, the solid-state sample based on cobaltous porphyrin exhibits remarkable instability; storage in



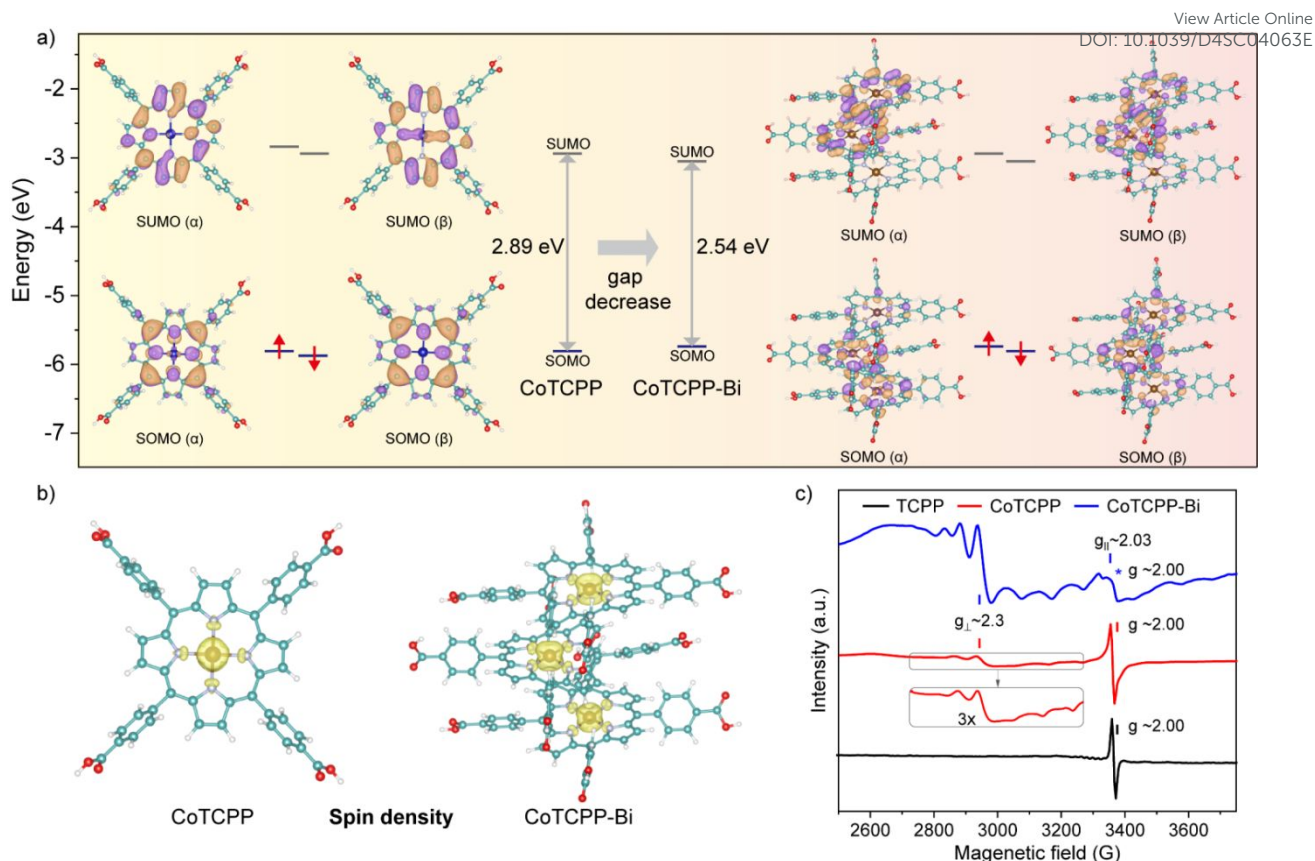


Figure 3. (a) Frontier molecular orbital diagrams of CoT CPP and CoT CPP-Bi. (b) Spin density maps of CoT CPP and CoT CPP-Bi. (c) EPR spectra of solid-state samples of T CPP, CoT CPP and CoT CPP-Bi collected at 100 K.

air or some common solvents can result in the absence or alteration of EPR signaling. Prior studies have typically shielded cobaltous porphyrins from axial ligation by storing them in a vacuum or under an inert atmosphere, or by embedding them in solid-state diamagnetic matrices.^{4,22} In this work, the hyperfine coupling between unpaired electrons and the $I = 7/2$ ^{59}Co nucleus in CoT CPP-Bi produces a distinct eight-line splitting signal, characteristic of a well-known Co^{II} -based metalloradical.²³ Whereas, CoT CPP displays a weaker signal related to the Co^{II} metalloradical. Comparison of experimental and theoretical data enabled the determination of spin-Hamiltonian parameters: $S = 1/2$, $g_{\perp} = 2.3$, $g_{\parallel} = 2.03$, consistent with values previously reported for the Co^{II} center with a four-coordination environment, as indicated by XRD. Accordingly, the CoT CPP-Bi powder was intentionally exposed to air for an extended period, resulting in the observation of an intense radical signal, which could be ascribed to the closely spaced metalloporphyrinic arrays within the model. This is supported by the more prominent Co^{II} -based metalloradical signal in CoT CPP-Bi compared to CoT CPP. Heating CoT CPP-Bi results in a singular broad resonance signal, while lower temperatures yield a more complex pattern with split peak formations (Figure S19). Conversely, the free-radical signal peaks with $g = 2$ consistently dominated in the samples T CPP and CoT CPP (Figures S20 and S21). CoT CPP-Bi serves as a

model capable of stabilizing single-electron spins in the Co^{II} center by preventing axial coordination.

As previously stated, the formation of robust and precisely arranged aggregations of the compound CoT CPP-Bi diminishes the energy gap between the S_0 and S_1 states, allowing for increased light absorption in the NIR region. Figure S22 illustrates that the reduced bandgap of CoT CPP-Bi no longer matches the energy level of visible fluorescence, leading to fluorescence quenching, which promotes the conversion of NIR light into thermal energy. Moreover, the maintenance of air-stable functionality in organic conjugated radicals is vital for photothermal conversion, given their general susceptibility to oxygen. However, when these radicals are integrated into well-designed materials or systems, they can retain their functionality in air, which is essential for their practical application in photothermal devices. The effective aggregation of cobalt porphyrins produces plentiful and vigorous Co^{II} -based metalloradicals that can attenuate radiative transitions, thus intensifying non-radiative processes.

Photothermal conversion performance

Leveraging its outstanding structural stability, UV-Vis-NIR absorption, and the abundance of Co^{II} -based metalloradicals, CoT CPP-Bi appears to possess remarkable photothermal conversion properties. Figure 4a shows the temperature change of CoT CPP-Bi powder when exposed to a 0.7 W cm^{-2} 808 nm laser for 50 seconds, monitored by an IR thermal



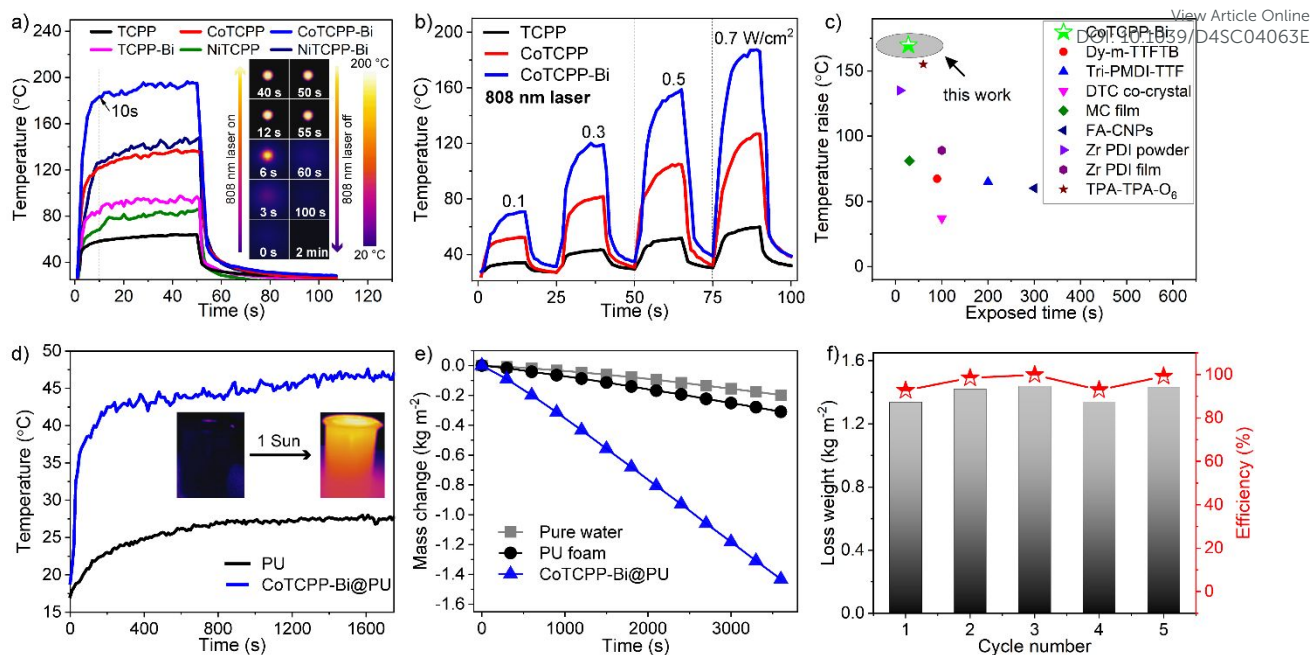


Figure 4. (a) Photothermal conversion curves of TCPP, CoTCPP, CoTCPP-Bi, TCPP-Bi, NiTCPP, and NiTCPP-Bi under irradiation of 0.7 W cm⁻² 808 nm laser. Insert: IR-thermal images of CoTCPP-Bi under irradiation of 0.7 W cm⁻² 808 nm laser. (b) Heating and cooling cycles for TCPP, CoTCPP and CoTCPP-Bi under different energy power 808 nm lasers. (c) Temperature variations for CoTCPP-Bi and some typical solid-state photothermal materials reported under 808 nm laser of 0.7 W cm⁻². (d) Photothermal conversion behavior of PU and CoTCPP-Bi-loaded PU foams under 1 sun light irradiation (1 kW m⁻²) (e) Water evaporation curves with pure water, PU foam and CoTCPP-Bi-loaded PU under simulated sunlight with an intensity of 1 kW m⁻² (1 sun). (f) Evaporation rate and efficiency for CoTCPP-Bi-loaded PU in five cycles.

camera. Upon laser exposure, the temperature swiftly rose from room temperature (rt) to approximately 150 °C within just 10 seconds, peaking at 190 °C within 30 seconds. Subsequently, upon deactivation of the laser, the temperature rapidly dropped back to ambient levels. Under a comparable experimental setup, TCPP demonstrated a modest maximum temperature of 62 °C, while NiTCPP, TCPP-Bi, CoTCPP, and NiTCPP-Bi exhibited a notably higher maximum temperature of 81 °C, 94 °C, 130 °C, and 140 °C, respectively. These results suggest that the introduction of metallized porphyrins and denser organization of metalloporphyrins have led to an improved photothermal performance. Additionally, the temperatures of TCPP, CoTCPP, and CoTCPP-Bi consistently increased as the irradiation power of the 808 nm laser increased, spanning intensities of 0.1, 0.3, 0.5, and 0.7 W cm⁻² (Figure 4b and Figure S23). It is noteworthy that the temperature variations displayed a strong linear relationship with the laser's power density, demonstrating exceptional thermal regulation capabilities (Figure S24). These findings emphasize the remarkable photothermal conversion efficiency of CoTCPP-Bi, surpassing that of most recently reported MOFs and other types of materials with NIR photothermal transformation (Figure 4c and Table S2).^{2a,24} Following ten cycles of laser irradiation on CoTCPP-Bi, with the laser being on and off alternately after each cycle, no notable photobleaching or temperature loss was detected via photothermal assessment (Figure S25). Furthermore, PXRD analysis confirmed the retention of its crystalline structure in the sample, signifying the excellent photostability of CoTCPP-Bi (Figure S26).

Interfacial solar vapor generation (ISVG) technology is a sustainable, environmentally friendly, and low-carbon alternative for seawater and wastewater treatment, offering a promising replacement for conventional desalination and purification techniques like reverse osmosis and ultrafiltration.²⁵ Upon exposure to a xenon lamp irradiation (1 kW m⁻², filtered to match the AM1.5G solar spectrum), the CoTCPP-Bi powder, with its enhanced NIR light absorption, registers a temperature rise from ambient to a peak of 60 °C. Conversely, the TCPP-Bi powder achieves a maximum temperature of 40 °C under the same experimental parameters (Figure S27). The impressive photothermal conversion capabilities of CoTCPP-Bi prompts us to assess its suitability for solar-driven water evaporation. Specifically, 30 mg of CoTCPP-Bi powder was loaded onto a commercially available white hydrophilic porous polyurethane (PU) to produce a brownish-black PU sponge. This sponge served as a foundation for establishing an efficient interfacial evaporation system, positioned atop the water to facilitate heat transfer (Figures S28 and S29). The solar-thermal conversion competence of CoTCPP-Bi@PU was recorded using an IR thermal camera under continuous irradiation of simulated sunlight (AM1.5 G, one sun with the light intensity of 1 kW m⁻²) for 30 minutes (Figure S30). The results revealed the effectiveness of CoTCPP-Bi@PU in promoting energy conversion at the water-air interface, as evidenced by the surface temperature of CoTCPP-Bi@PU reaching 45 °C while floating on the water, significantly higher than the pure PU temperature of 27 °C (Figure 4d). After one hour, the water temperature rose and equilibrated at 32.2 °C (Figure S31).



Mass change experiments were conducted to evaluate the efficacy of solar-driven water evaporation, involving time dependent water with PU foam and CoTCPP-Bi@PU (Figure 4e, Figure S32). Under 1-sun exposure in ambient conditions, the evaporation rate of CoTCPP-Bi@PU reached $1.43 \text{ kg m}^{-2} \text{ h}^{-1}$ and 98.5% solar-driven water evaporation efficiency (η), significantly outperforming PU ($0.2 \text{ kg m}^{-2} \text{ h}^{-1}$) and pure water ($0.1 \text{ kg m}^{-2} \text{ h}^{-1}$), as well as other photothermal materials (Table S3).^{24a,24f,25-26} The average solar-driven water evaporation efficiency (η) for CoTCPP-Bi@PU was determined to be 94% over five cycles (Figure 4f).

Conclusions

In conclusion, we synthesized a novel crystalline solid, through the combination of metalloporphyrin linkers with bismuth-carboxylate nodes. The stable Co^{II}-based metalloradical species and the robust aggregation of metalloporphyrins in CoTCPP-Bi, caused by π - π stacking between neighboring metalloporphyrins, impart strong absorption capabilities to the material in the NIR region. Consequently, under an energy density of 0.7 W cm^{-2} using an 808 nm laser, CoTCPP-Bi demonstrates remarkable photothermal conversion efficiency, achieving a temperature rise from rt to $190 \text{ }^\circ\text{C}$ within 30 seconds, and efficient solar-driven water evaporation, with an efficiency of 94% and a rate of $1.43 \text{ kg m}^{-2} \text{ h}^{-1}$ under 1 sun irradiation. This work highlights the potential for developing materials with superior photothermal conversion and NIR light absorption abilities by enhancing the aggregation and stabilization of metalloradical moieties. Furthermore, the integration of functional photothermal materials opens up new possibilities for the consolidation of photothermal water evaporation with multifunctional applications, thereby improving the versatility and efficiency of photothermal technologies.

Author Contributions

L. He carried out the experimental sections and wrote the manuscript. E. Chen and Q. Lin supervised the study and reviewed the manuscript. J. He helped the characterizations. All the authors discussed the results and contributed to the manuscript.

Conflicts of interest

There are no conflicts to declare.

Data availability

All experimental supporting data and procedures are available in the ESI.

Acknowledgements

This work was financially supported by the National Science

Foundation of China (22201283), the National Key Research and Development Project (2022YFA1503900), the National Science Foundation of Fujian Province (2022J05090, 2022T3008), Fujian Science & Technology Innovation Laboratory for Optoelectronic Information of China (2021ZR138) and the Open Project Program of the State Key Laboratory of Photocatalysis on Energy and Environment (SKLPEE-KF202204), Fuzhou University.

Notes and references

- a) H. Hu, H. Wang, Y. Yang, J.-F. Xu, X. Zhang, *Angew. Chem. Int. Ed.*, 2022, **61**, e202200799; b) Y. Wang, J. Zhang, W. Liang, H. Yang, T. Guan, B. Zhao, Y. Sun, L. Chi, L. Jiang, *CCS Chem.*, 2021, **4**, 1153; c) K. Li, X. Sun, Y. Wang, J. Wang, X. Dai, G. Li, H. Wang, *Nano Energy*, 2022, **93**, 106789; d) Q. Huang, X. Ye, W. Chen, X. Song, Y.-t. Chen, X. Wen, M. Zhang, Y. Wang, S.-L. Chen, L. Dang, M.-D. Li, *ACS Energy Lett.*, 2023, **8**, 4179; e) H.-C. Ma, C.-C. Zhao, G.-J. Chen, Y.-B. Dong, *Nat. Commun.*, 2019, **10**, 3368; f) D. Wang, Z. Zhang, L. Lin, F. Liu, Y. Wang, Z. Guo, Y. Li, H. Tian, X. Chen, *Biomaterials*, 2019, **223**, 119459; g) K. Zhang, X. Meng, Y. Cao, Z. Yang, H. Dong, Y. Zhang, H. Lu, Z. Shi, X. Zhang, *Adv. Funct. Mater.*, 2018, **28**, 1804634; h) J.-D. Xiao, H.-L. Jiang, *Acc. Chem. Res.*, 2019, **52**, 356.
- a) Z. Wang, J. Zhou, Y. Zhang, W. Zhu, Y. Li, *Angew. Chem. Int. Ed.*, 2022, **61**, e202113653; b) Z. Wang, F. Alkan, C. M. Aikens, M. Kurmoo, Z.-Y. Zhang, K.-P. Song, C.-H. Tung, D. Sun, *Angew. Chem. Int. Ed.*, 2022, **61**, e202206742; c) Y. Jiang, Y. Zhang, Y. Deng, S. Dong, B. Li, Y. Yi, Z. Zeng, H. Chen, H. Luo, Y. Geng, *CCS Chem.*, 2022, **4**, 3497; d) A. H. Proppe, Y. C. Li, A. Aspuru-Guzik, C. P. Berlinguette, C. J. Chang, R. Cogdell, A. G. Doyle, J. Flick, N. M. Gabor, R. van Grondelle, S. Hammes-Schiffer, S. A. Jaffer, S. O. Kelley, M. Leclerc, K. Leo, T. E. Mallouk, P. Narang, G. S. Schlau-Cohen, G. D. Scholes, A. Vojvodic, V. W.-W. Yam, J. Y. Yang, E. H. Sargent, *Nat. Rev. Mater.*, 2020, **5**, 828; e) G. Chen, J. Sun, Q. Peng, Q. Sun, G. Wang, Y. Cai, X. Gu, Z. Shuai, B. Z. Tang, *Adv. Mater.*, 2020, **32**, 1908537; f) B. Yang, Z. Zhang, P. Liu, X. Fu, J. Wang, Y. Cao, R. Tang, X. Du, W. Chen, S. Li, H. Yan, Z. Li, X. Zhao, G. Qin, X.-Q. Chen, L. Zuo, *Nature*, 2023, **622**, 499; g) M. E. Matter, L. Čamdžić, E. E. Stache, *Angew. Chem. Int. Ed.*, 2023, **62**, e202308648; h) O. Shelonchik, N. Lemcoff, R. Shimon, A. Biswas, E. Yehezkel, D. Yesodi, I. Hod, Y. Weizmann, *Nat. Commun.*, 2024, **15**, 1154.
- M. Chen, X. Zhang, J. Liu, F. Liu, R. Zhang, P. Wei, H. Feng, M. Tu, A. Qin, J. W. Y. Lam, D. Ding, B. Z. Tang, *ACS Nano*, 2020, **14**, 4265.
- a) X. Chen, H. Xie, E. R. Lorenzo, C. J. I. V. Zeman, Y. Qi, Z. H. Syed, A. E. B. S. Stone, Y. Wang, S. Goswami, P. Li, T. Islamoglu, E. A. Weiss, J. T. Hupp, G. C. Schatz, M. R. Wasielewski, O. K. Farha, *J. Am. Chem. Soc.*, 2022, **144**, 2685; b) H. Gao, X. Zhi, F. Wu, Y. Zhao, F. Cai, P. Li, Z. Shen, *Angew. Chem. Int. Ed.*, 2023, **62**, e202309208.
- L. Zhao, X. Ren, X. Yan, *CCS Chem.*, 2021, **3**, 678.
- C. Preston-Herrera, S. Dadashi-Silab, D. G. Oblinsky, G. D. Scholes, E. E. Stache, *J. Am. Chem. Soc.*, 2024, **146**, 8852.
- a) F. Würthner, T. E. Kaiser, C. R. Saha-Möller, *Angew. Chem. Int. Ed.*, 2011, **50**, 3376; b) Y.-Z. Chen, Z. U. Wang, H. Wang, J. Lu, S.-H. Yu, H.-L. Jiang, *J. Am. Chem. Soc.*, 2017, **139**, 2035.
- Q. Zou, M. Abbas, L. Zhao, S. Li, G. Shen, X. Yan, *J. Am. Chem. Soc.*, 2017, **139**, 1921.
- a) T. Yamaguchi, T. Kimura, H. Matsuda, T. Aida, *Angew. Chem. Int. Ed.*, 2004, **43**, 6350; b) B. Guo, G. Feng, P. N. Manghnani, X. Cai, J. Liu, W. Wu, S. Xu, X. Cheng, C. Teh, B. Liu, *Small*, 2016, **12**, 6243; c) Q. Yin, E. V. Alexandrov, D.-H.



- Si, Q.-Q. Huang, Z.-B. Fang, Y. Zhang, A.-A. Zhang, W.-K. Qin, Y.-L. Li, T.-F. Liu, D. M. Proserpio, *Angew. Chem. Int. Ed.*, 2022, **61**, e202115854.
- 10 a) C. Röger, Y. Miloslavina, D. Brunner, A. R. Holzwarth, F. Würthner, *J. Am. Chem. Soc.*, 2008, **130**, 5929; b) S. Ganapathy, S. Sengupta, P. K. Wawrzyniak, V. Huber, F. Buda, U. Baumeister, F. Würthner, H. J. M. de Groot, *Proc. Natl. Acad. Sci.*, 2009, **106**, 11472.
- 11 X. Zhang, M. C. Wasson, M. Shayan, E. K. Berdichevsky, J. Ricardo-Noordberg, Z. Singh, E. K. Papazyan, A. J. Castro, P. Marino, Z. Ajoyan, Z. Chen, T. Islamoglu, A. J. Howarth, Y. Liu, M. B. Majewski, M. J. Katz, J. E. Mondloch, O. K. Farha, *Coord. Chem. Rev.*, 2021, **429**, 213615.
- 12 L. Yang, P. Cai, L. Zhang, X. Xu, A. A. Yakovenko, Q. Wang, J. Pang, S. Yuan, X. Zou, N. Huang, Z. Huang, H.-C. Zhou, *J. Am. Chem. Soc.*, 2021, **143**, 12129.
- 13 a) Z. Wang, Z. Zeng, H. Wang, G. Zeng, P. Xu, R. Xiao, D. Huang, S. Chen, Y. He, C. Zhou, M. Cheng, H. Qin, *Coord. Chem. Rev.*, 2021, **439**, 213902; b) E. P. Gómez-Oliveira, D. Reñares-Fisac, L. M. Aguirre-Díaz, F. Esteban-Betegón, M. Pintado-Sierra, E. Gutiérrez-Puebla, M. Iglesias, M. Ángeles Monge, F. Gándara, *Angew. Chem. Int. Ed.*, 2022, **61**, e202209335.
- 14 K. Ni, T. Luo, G. Lan, A. Culbert, Y. Song, T. Wu, X. Jiang, W. Lin, *Angew. Chem. Int. Ed.*, 2020, **59**, 1108.
- 15 M. M. Olmstead, D. A. Costa, K. Maitra, B. C. Noll, S. L. Phillips, P. M. Van Calcar, A. L. Balch, *J. Am. Chem. Soc.*, 1999, **121**, 7090.
- 16 M. Rossi, J. P. Glusker, L. Randaccio, M. F. Summers, P. J. Toscano, L. G. Marzilli, *J. Am. Chem. Soc.*, 1985, **107**, 1729.
- 17 a) D. V. Konarev, S. S. Khasanov, A. Otsuka, Y. Yoshida, G. Saito, *J. Am. Chem. Soc.*, 2002, **124**, 7648; b) P. D. W. Boyd, M. C. Hodgson, C. E. F. Rickard, A. G. Oliver, L. Chaker, P. J. Brothers, R. D. Bolskar, F. S. Tham, C. A. Reed, *J. Am. Chem. Soc.*, 1999, **121**, 10487.
- 18 D. Xie, S. Wang, S. Li, W. Yang, Y.-S. Feng, *Catal. Sci. Technol.*, 2022, **12**, 3254.
- 19 I. Strauss, A. Mundstock, D. Hinrichs, R. Himstedt, A. Knebel, C. Reinhardt, D. Dorfs, J. Caro, *Angew. Chem. Int. Ed.*, 2018, **57**, 7434.
- 20 a) S. Van Doorslaer, A. Schweiger, *Phys. Chem. Chem. Phys.*, 2001, **3**, 159; b) T. Yamabayashi, M. Atzori, L. Tesi, G. Cosquer, F. Santanni, M.-E. Boulon, E. Morra, S. Benci, R. Torre, M. Chiesa, L. Sorace, R. Sessoli, M. Yamashita, *J. Am. Chem. Soc.*, 2018, **140**, 12090.
- 21 A. T. Gallagher, C. D. Malliakas, T. D. Harris, *Inorg. Chem.*, 2017, **56**, 4654.
- 22 F. Ann Walker, *J. Magn. Reson.*, 1974, **15**, 201.
- 23 a) J. A. de Bolfo, T. D. Smith, J. F. Boas, J. R. Pilbrow, *J. Chem. Soc., Dalton Trans.*, 1976, 1495; b) Y.-N. Gong, W. Zhong, Y. Li, Y. Qiu, L. Zheng, J. Jiang, H.-L. Jiang, *J. Am. Chem. Soc.*, 2020, **142**, 16723.
- 24 a) X. Ye, L.-H. Chung, K. Li, S. Zheng, Y.-L. Wong, Z. Feng, Y. He, D. Chu, Z. Xu, L. Yu, J. He, *Nat. Commun.*, 2022, **13**, 6116; b) J. Su, P. Cai, T. Yan, Z.-M. Yang, S. Yuan, J.-L. Zuo, H.-C. Zhou, *Chem. Sci.*, 2022, **13**, 1657; c) J. Su, N. Xu, R. Murase, Z.-M. Yang, D. M. D'Alessandro, J.-L. Zuo, J. Zhu, *Angew. Chem. Int. Ed.*, 2021, **60**, 4789; d) B. Lü, Y. Chen, P. Li, B. Wang, K. Müllen, M. Yin, *Nat. Commun.*, 2019, **10**, 767; e) Y. Wang, W. Zhu, W. Du, X. Liu, X. Zhang, H. Dong, W. Hu, *Angew. Chem. Int. Ed.*, 2018, **57**, 3963; f) S. Zhou, X. Kong, M. Strømme, C. Xu, *ACS Mater. Lett.*, 2022, **4**, 1058.
- 25 X. Q. Li, J. L. Li, J. Y. Lu, N. Xu, C. L. Chen, X. Z. Min, B. Zhu, H. X. Li, L. Zhou, S. N. Zhu, T. J. Zhang, J. Zhu, *Joule*, 2018, **2**, 1331.
- 26 a) X. Yan, S. Lyu, X.-Q. Xu, W. Chen, P. Shang, Z. Yang, G. Zhang, W. Chen, Y. Wang, L. Chen, *Angew. Chem. Int. Ed.*, 2022, **61**, e202201900; b) J. Liu, Y. Cui, Y. Pan, Z. Chen, T. Jia, C. Li, Y. Wang, *Angew. Chem. Int. Ed.*, 2022, **61**, e202117087; c) X. Tang, Z. Chen, Q. Xu, Y. Su, H. Xu, S. Horike, H. Zhang, Y. Li, C. Gu, *CCS Chem.*, 2021, **4**, 2842; d) Q. Ma, P. Yin, M. Zhao, Z. Luo, Y. Huang, Q. He, Y. Yu, Z. Liu, Z. Hu, B. Chen, H. Zhang, *Adv. Mater.*, 2019, **31**, 1808249.



Data availability

All experimental supporting data and procedures are available in the ESI.

